Sustainable Energy & Fuels

In-Situ Formed Lithiophilic Ni3S2@Ni Current Collector for Stable Lithium Metal Batteries

Journal:	*Sustainable Energy & Fuels*
Manuscript ID	SE-ART-06-2023-000798.R1
Article Type:	Paper
Date Submitted by the Author:	08-Aug-2023
Complete List of Authors:	Qi, Mengpei; Henan University of Technology Xie, Lingling; Henan University of Technology, School of Environmental Engineering Han, Qing ; Henan University of Technology Qiu, Xuejing ; Henan University of Technology Katiyar, Swati; University of Puerto Rico Liu, Xinhua; Imperial College London, Dyson School of Design Engineering; Beihang University, School of Transportation Science and Engineering Yang, Shichun; Beihang University, School of Transportation Science and engineering Zhu, Limin; Henan University of Technology, School of Chemistry and Chemical Engineering Wu, Xianyong; Oregon State University Chen, Libao; Central South University Cao, Xiaoyu; Henan University of Technology, School of Chemistry and Chemical Engineering

In-Situ Formed Lithiophilic Ni_3S_2@Ni Current Collector for Stable Lithium Metal Batteries

Mengpei Qi,[a,c] Lingling Xie,[b,c] Qing Han,[a,c] Xuejing Qiu,[b,c] Swati Katiyar,[d] Xinhua Liu,[e] Shichun Yang,[e] Limin Zhu,[a,c,*] Xianyong Wu,[d,*] Libao Chen,[f,*] Xiaoyu Cao [a,c,*]

[a] School of Chemistry and Chemical Engineering, Henan University of Technology, Zhengzhou 450001, PR China

[b] School of Environmental Engineering, Henan University of Technology, Zhengzhou 450001, PR China

[c] Key Laboratory of High Specific Energy Materials for Electrochemical Power Sources of Zhengzhou City, Henan University of Technology, Zhengzhou 450001, China

[d] Department of Chemistry, University of Puerto-Rico, Rio Piedras Campus, San Juan, PR, 00925, USA

[e] School of transportation Science and Engineering, Beihang University, Beijing, 100191, China

[f] State Key Laboratory for Powder Metallurgy, Central South University, Changsha 410083, China

* Corresponding author

E-mail address: lmzhu@haut.edu.cn (L. Zhu), xianyongwu2020@gmail.com (X. Wu), lbchen@csu.edu.cn (L. Chen), caoxy@haut.edu.cn (X. Cao)

Abstract

Attracting immense interest as the lithium storage material, lithium metal anodes boast the highest specific capacity of 3860 mAh g^{-1}, lowest redox potential of -3.04 V, compared to standard hydrogen electrodes and sustainability. Nevertheless, extreme dendrite growth, the severe lithium deposition, and enormous volume alteration have

serious impeded the practical progress of lithium anodes. To address these problems, researchers have proposed to construct three-dimensional (3D) current collectors, which can adjust the Li deposition and improve cycle stability. Herein, we *in-situ* grow lithiophilic Ni_3S_2 nanowire arrays on a porous nickel current collector (hereinafter denoted as Ni_3S_2@Ni) by a simple hydrothermal reaction, which significantly improved the Li metal anode performance. This Ni_3S_2@Ni composite current collector has a relatively uniform and open micro-nano structure, which facilitates the Li^+ ion migration/diffusion and also improves the electrode-electrolyte interfacial properties. In addition, the Ni_3S_2@Ni composite current collector achieves a prolonged lithium plating/stripping lifespan of 900 hours at 2 mA cm^{-2} without short circuit in symmetrical batteries. Furthermore, the full cell assembled with composite current collector and $LiFePO_4$ cathode demonstrates outstanding cycling stability, where the capacity retention is 80.6% after 500 cycles at 1 C. Our proposed 3D Ni_3S_2@Ni composite current collector will further boost the development of the stable Li metal anode.

Keywords: Li metal batteries, 3D current collectors, Ni_3S_2@Ni composite, Anode materials, Cycling stability

1. Introduction

Since their initial commercialization in the 1990s, lithium-ion batteries (LIBs) have been widely employed in electric vehicles as well as other applications owing to the advantageous properties of high energy density, extended cycling life, light weight, and low self-discharge [1]. However, LIBs have approached to their energy density upper limit (~250 Wh kg^{-1}), which cannot satisfy the increasing energy demand from our modern society. For instance, electric vehicles suffer from a short mileage problem, which cannot compete with the gasoline cars [2].To increase the battery energy density, researchers have worked to investigate high-capacity batteries materials, such as NMC811, Li-rich cathode, sulfur, and alloy materials (Si, Sn, Sb) [3-6]. The lithium metal anode, with its theoretical capacity of (3860 mAh g^{-1}), lowest redox potential of (-3.04

V), is particularly promising for the energy storage systems [7-9]. Furthermore, the lithium metal could be directly coupled with Li-deficient cathode materials for lithium-sulfur batteries [10-12].It has been suggested that Li metal batteries could realize a high energy of 300-500 Wh kg^{-1}, which is much higher than LIBs [13, 14]. Therefore, lithium metal batteries have made high performance battery accessible both academic and industry in recent years.

Nevertheless, the lithium metal as an anode material, which greatly hinder its further commercialization. Firstly, the Li metal exhibits the ultra-low redox potential and high reactivity, which cause serious side reactions with carbonate/ether electrolytes. Consequently, it leads to the low Coulombic efficiency (CE) and electrolyte dry-up after long cycling [15, 16]. Secondly, a bare lithium metal without a support produces significant volume expansion/shrinkage, which results in the electrode cracking and further pulverization. Lastly, the Li metal is prone to an uneven deposition process during the repeated plating/striping cycles, which results in the unwanted lithium dendrite growth [17, 18]. As a result, the battery short circuit will occur, leading to a severe safety concern, which could impede the practical development of lithium metal batteries.

To address these issues, extensive insights have been proposed to optimize the lithium metal anode performance, which includes developing innovative electrolytes or electrolyte additives [19-22], modifying the electrode interface [23-25], and developing three-dimensional (3D) current collectors [26-28], constructing artificial solid-electrolyte interface (SEI), and separator modification [29, 30]. Among these methods, the design of 3D current collectors has received wide attention, owing to the advantages of introducing a lithiophilic surface, regulating the Li metal deposition, and buffering the volume change.[31-33] For example, Shi *et al.*[34] used nitrogen-doped graphene to modify the 3D porous copper, which facilitated a uniform Li^+ flux for the electrochemical reaction, thereby suppressing the lithium dendrites. Hu *et al.* [35] prepared a hierarchically structured Cu@VG of graphene nanowalls, which were grown directly on three-dimensional copper foam in the vertical direction. Due to the lithiophilic nature of this current collector, they achieved dendrite-free Li metal plating and demonstrated a high

CE of ~99.0%. Yang *et al.*[36] treated the porous Cu foam by surface oxidization, which was further compressed by roller compression. This current collector demonstrated preferential lithium surface affinity and ensure uniform lithium deposition. Li *et al.*[37] used self-assembling as fabricated graphene oxide (rGO) to consolidate the planar Li layer. Due to the Li-rGO lattice matching, the Li atoms preferentially grow along the (110) plane direction, which leads to a planar Li deposition morphology. All these reports indicate that it is effective to improve the lithium metal anode performance by developing suitable 3D current collectors [38].

Herein, we used a hydrothermal strategy to *in-situ* grow a lithiophilic Ni_3S_2 nanowire-array layer on the porous nickel skeleton (hereinafter referred to Ni_3S_2@Ni), which serves as a high-performance and porous 3D current collector for lithium metal anode. We discover that this current collector is beneficial to interact with Li^+ ions, as revealed by the material phase characterization, electrochemical testing, and density functional theory (DFT) calculations. This Ni_3S_2@Ni composite collector exhibits a relatively uniform and open micro/nano structures, which are conducive to the rapid diffusion and migration of lithium ions, thus leading to excellent electrochemical properties in symmetric Li||Li batteries and $LiFePO_4$-based full cells. Specifically, in symmetrical batteries, the Ni_3S_2@Ni current collector achieved excellent cycling stability of 900 hours at 2 mA cm^{-2}. The full battery delivered an impressive capacity retention of 80.6% after 500 cycles with the $LiFePO_4$ cathode. Due to the lithiophilic properties and high surface area, the outstanding performance of the Ni_3S_2@Ni current collectors is obtained, which can promote the uniform Li deposition and reduce the volume change. Our work further enriches the variety of 3D current collectors, which are beneficial for the future implementation of lithium metal anode in battery applications.

2. Experimental section

2.1 Fabrication of the lithiophilic 3D Ni_3S_2@Ni current collector

The 3D porous nickel skeleton (S-Ni 900) current collector was first prepared by

a powder metallurgy loose sintering method, which has been washed to purify the impurities. Specifically, the commercial carbonyl nickel powder with a particle size of 8−10 μm is laid flat in a circular groove in the middle of a corundum mold with an inner diameter of 16 mm and a depth of 0.5 mm, so that the powder is level with the mold surface, and the vibrating powder is filled in the groove. Then, the mold was transferred to the high temperature zone of the tube furnace for vacuum calcination, heated to 900 °C, respectively, and kept warm for 2 h at a heating rate of 10 °C min^{-1}, and cooled to room temperature to obtain a three-dimensional porous nickel skeleton material. Subsequently, this nickel skeleton was placed in a 100 mL Teflon lined stainless steel autoclave with a solution of 0.0063 g Thioacetamide (CH_3CSNH_2, TAA) dissolved in 80 mL distilled water. The reaction was maintained at 150℃ in an oven for 2 h. Finally, the target products Ni_3S_2@Ni composite current collectors were obtained after drying at vacuum 80 °C for 12 h.

2.2 Material characterization

The XRD（X Ray Diffraction）technique, a widely-employed characterization method, is employed to verify the structure and phase of materials. In this work, we used the Rigaku XRD to study the material crystal structure. The target used in the testing process is Cu target, the light source is K_α-ray with a wavelength of $\lambda = 1.54056$ Å. The testing range is 10-90°, and the scanning speed is 10° min^{-1}. Scanning electron microscopy (SEM) can obtain information on the material morphology and the particle size. Here we used the SU8010 SEM analyzer. When lithium was not deposited, we could directly observe the microstructure of the original current collector. However, in order to observe the lithium deposition morphology on the current collector, it is necessary to disassemble the battery, retrieve the electrode, and use dimethyl ether (DME) to wash away the residual surface electrolyte. After drying, we used a cold field emission SEM with a vacuum transition chamber to observe the Li metal morphology. Note that the Li metal should be quickly transferred to the testing chamber to avoid oxidization. X-ray photoelectron spectroscopy (XPS) can be employed to assess

valance state and chemical bonding information on the material surface. Here, the sample tests were carried out by Thermo Scientific K-Alpha XPS instrument, and the sample size is less than 5 *5 *3 mm in the glove box, which can avoid contacting with air. The obtained data is fitted by the Avanage software, and the binding energy is corrected to the standard C 1s position at 284.8 eV.

2.3 Electrochemical tests

Using CR2016 coin cells as the working electrodes, the Ni_3S_2@Ni composite and the bare S-Ni 900 current collectors were both assembled, with Li foil (0.6 mm in thickness) and Celgard 2400 microporous polypropylene film serving as the counter electrodes and separator, respectively. The electrolyte was 1 M lithium bis(trifluoromethanesulfonyl)imide (LiTFSI) in a solvent mixture of 1,3-dioxolane (DOL) and 1,2-dimethoxyethane (DME) (volume ratio: 1: 1) supplemented with 2% $LiNO_3$ additives. The electrolyte volume was ~150 μL in each battery. In an argon-filled glove box, the Neware CT-ZWJ-4'S-T-1U multichannel battery system was utilized to test the batteries that had been assembled. Before the Li metal plating testing, the battery was cycled at 0.01-0.1 V (*vs.* Li^+/Li) at 50 mA for 5 cycles to stabilize the SEI layer. The coulombic efficiency test featured a constant Li (1 mA h cm^{-2}) capacity plated on the substrate, which was then stripped away to 1 V at either 1 or 2 mA cm^{-2} for each cycle. Symmetrical cells were tested to evaluate the cyclic stability of lithium electrodes by a quantitative plating/stripping process. A certain amount of the lithium was pre-deposited on the current collector surface and retrieved from the battery, which was further assembled into a symmetrical battery for electrochemical testing.

In Li|$LiFePO_4$ full cells, the composite anode was obtained by pre-plating Li on Ni or Ni_3S_2@Ni current collector, which was then paired with the $LiFePO_4$ cathode. Mixed together in N-methyl-2-pyrrolidone (NMP) was $LiFePO_4$ powders, PVDF, and conductive carbon (mass ratio: 8:1:1) to form a slurry for the cathode's preparation, which was then casted onto an aluminum foil. The NMP solvent was removed by vacuum drying at 110℃ for 12 h. The full cells were cycled between 2.4 V and 4.2 V to test the cycling property. To evaluate the rate performance, the cells were cycled at

0.1 C, 0.5 C, 1 C, 2 C, 5 C, and 0.1 C. The 1 C rate is defined as ~170 mA g^{-1} based on the theoretical capacity of $LiFePO_4$.

3. Results and discussion

3.1 Characterization of Ni_3S_2@Ni Composite Current Collector

Figure 1a schematically depicts the fabrication process of the Ni_3S_2@Ni composite current collector and its effect on the Li plating/stripping behavior. The sintered nickel (S-Ni 900) current collector was prepared by powder metallurgy and washed thoroughly with distilled water and ethanol at 900℃ [5, 39]. A hydrothermal reaction of sintered nickel in TAA and distilled water was utilized to create the Ni_3S_2@Ni composite current collector [40, 41]. This 3D structure composite current collector exhibits a moderate pore size and sufficient pore volume, which guarantees the smooth transportation of Li^+ ions. More importantly, due to the presence of a lipophilic Ni_3S_2 layer, the initial nucleation could be significantly improved. Additionally, the ample space in the 3D current collector could buffer the volume change, which further enhances the ion/electron transport. In comparison, without the lipophilic Ni_3S_2 layer, a random Li nucleation and growth will happen, which leads to severe dendrite growth on the S-Ni 900 current collector (**Figure 1b**).

The structure of the *in-situ* grown Ni_3S_2 nanoarray on the S-Ni 900 substrate was determined by XRD (**Figure 2a**). As shown, there are four diffraction peaks at 30.89°, 37.88°, 44.47°, and 55.31°, which correspond to the (110), (111), (120) and (121) planes of Ni_3S_2 crystals, respectively. Meanwhile, there are three peaks at 44.47°, 50.25° and 77.17°, which are attributed to the (111), (200) and (220) planes of nickel, respectively. The above XRD results show that we successfully loaded Ni_3S_2 on the three-dimensional nickel skeleton S-Ni 900 by the hydrothermal reaction, which agrees well with the previous report [42].

To verify the existence of Ni_3S_2 and the chemical state change of nickel, we carried out XPS tests on the sample current collectors before and after the modification. **Figure 2b** shows the XPS total spectrum of two samples, where the S2p peak appears in the

modified Ni_3S_2@Ni sample. **Figure 2c-d** show the high-resolution Ni 2p spectra of S-Ni 900 and Ni_3S_2@Ni current collectors, where the valance state of nickel changed significantly before and after the modification. Firstly, the characteristic peaks at 853.5 and 875.6 eV in the sintered nickel samples disappeared after modification, which correspond to Ni^+. The bonding of nickel to carbon occurs during carbonyl cracking of the original carbonyl nickel powder. As a result, it is oxidized to a higher nickel valence state during the hydrothermal process. The peak strength at ~855.9 eV increased significantly after modification, possibly due to the presence of a trace amount of NiO on the S-Ni 900 surface, where Ni_3S_2@Ni was generated in large quantities. Furthermore, the chemical state of nickel in NiO and Ni_3S_2@Ni is not much different, and the combination of XPS peaks is close to that of the characteristic peaks, resulting in a significant increase in the peak strength. The XPS spectrum of the S2p spectra of the Ni_3S_2@Ni sample, depicted in **Figure 2e**, displays two peaks at 161.2 eV and 162.2 eV, which are respectively S 2p3/2 and S 2p1/2. The peak at 163.3 eV could be due to the C_2H_5NS that remains after the synthesis.

The morphology of the 3D nickel skeleton collector (S-Ni 900) and the Ni_3S_2@Ni composite collectors prepared at different TAA concentrations were observed by scanning electron microscopy (SEM). Herein, depending on the amount of TAA input, a series of composite current collectors are generated. For convenience, the corresponding Ni_3S_2@Ni composite current collector is named after the abbreviations 1/8 Ni_3S_2@Ni, 1/24 Ni_3S_2@Ni and 1/48 Ni_3S_2@Ni, respectively. In **Figure 3** (A1-A3), the S-Ni 900 has a smooth surface and has almost no edges and corners. The pore size is around 5 μm. **Figure 3** (B1-B3) shows the SEM images of a 1/8 Ni_3S_2@Ni composite (1/8 of the initial sulfur source concentration), which mainly exhibits a rough surface with irregular nano-sized particles. Whereas, the particle agglomeration is not conducive to diffusion of lithium ions. **Figure 3** (C1-C3) displays the SEM images of the 1/24 Ni_3S_2@Ni spherical composites, which are composed of uniform nanoparticles with the beads arranged tightly and uniformly distributed. This structure is beneficial to the fast Li^+ ion transport and electrolyte wetting. In addition, its open and porous structure also provides more active sites for electrochemical reactions. **Figure 3** (D1-

D3) shows the SEM images for the 1/48 Ni_3S_2@Ni composite, where the hexagonal flake nanoarray modified nickel substrate can be clearly seen. It is likely that less Ni_3S_2 grown in situ in the S-Ni 900 current collector as the sulfur source concentration decreases. As will be discussed later, the spherical 1/24 Ni_3S_2@Ni current collector improves the interface properties and thus the lithium metal batteries show good magnification performance and cycle stability performance.

3.2 Mitigation of the Volume Change

We assembled symmetrical cells and used SEM to compare the effect of S-Ni 900 and 1/24 Ni_3S_2@Ni current collectors on the lithium plating. The current density is 2 mA cm^{-2} and the area capacity is fixed at 1 mAh cm^{-2}. **Figure 4a** (A1-A3) shows initial lithium deposition morphology on the 1/24 Ni_3S_2@Ni current collector at different magnifications, which exhibits a smooth structure with a uniform particle distribution. After 1 and 45 cycles, as shown in **Figure 4a** (B1-B3) and **Figure 4a**(C1-C3), the surface of the Ni_3S_2@Ni is still relatively smooth, and no obvious lithium dendrites appear. In contrast, the S-Ni 900 current collector has some dendrites on their surface after the initial deposition of lithium, as shown in **Figure 4b** (A1-A3). After the first cycle (**Figure 4b** B1-B3), an extremely amount of lithium dendrites are produced inside the skeleton. After 45 cycles, the intersecting dendrites can be clearly seen on its surface (**Figure 4b** C1-C3), resulting in a loose and porous surface. Note that the appearance of this porous layer is not favorable to the diffusion of lithium ions, the battery will be short-circuited eventually with the production of lithium dendrites.

The *in-situ* lithiophilic porous skeleton acts as the "host" for lithium metal, which can maintain the integrity and stability of the electrode structure. To verify the ability to mitigate volume change, we observed the cross-section morphology of the current collectors, as displayed in **Figure 4c**(A-C), the Ni_3S_2@Ni current collector is covered by a layer of silvery white lithium at the electrode top after different cycles, and the lithium is relatively flat and evenly distributed across the cross-section. The cross-section thickness after the initial deposition of lithium was 376.71 μm, which was reduced to 338.18 μm after the 1^{st} cycle and slightly reduced to 330.91 μm in the 45^{th}

cycle. The cross-section SEM images of the S-Ni 900 current collector are shown in **Figure 4c**(D-F). The thickness after the initial lithium deposition is 404.92 μm, which was reduced to 362.41 μm after one cycle. After 45 cycles, the lithium electrode has been partially collapsed, resulting in a reduction in thickness to 348.34 μm. The reason for the volume variation is that the porosity between the S-Ni 900 collector backbone will decrease during the lithium deposition/dissolution, therefore, more lithium cannot be deposited in the S-Ni 900 collector pores, which is clogged on the surface. With more lithium deposition, more lithium accumulation on the nickel skeleton surface will happen, which can cause the rapid growth of lithium dendrites or "dead Li" [43-45]. The comparison here has verified the effect of Ni_3S_2@Ni in alleviating the volume change and improving the electrode stability.

3.3 Symmetrical Battery Performance of Ni_3S_2@Ni Composite Current Collector and Li

The electrochemical performance of the half-cell- and symmetrical cells assembled with either Ni_3S_2@Ni composite current collector or S-Ni 900 current collector is compared in Figure 5. In **Figure 5**(a), the nucleation overpotential of the Ni_3S_2@Ni is 36 mV, while the nucleation overpotential of the S-Ni 900 is as high as 98 mV, which indicates that the Ni_3S_2@Ni can effectively reduce the nucleation energy barrier and promote faster reaction kinetics. **Figure 5**b-c shows the charge/discharge curves of the 1/24 Ni_3S_2@Ni composite current collector at 2 mA cm^{-2}, where the plating capacity is 1mAh cm^{-2}. In addition, the nucleating potential η1 of 1/24 Ni_3S_2@Ni is 61.6 mV, and the growth potential η2 is 46.54 mV, then the nucleating potential of 1/24 Ni_3S_2@Ni composite collector is 15.1 mV. $|\eta 1|>|\eta 2|$, which means that Li^+ deposits a lower barrier to reduce to metal Li on a 1/24 Ni_3S_2@Ni composite collector, and thus 1/24 Ni_3S_2@Ni has a stronger lithogenicity [46, 47].

Batteries of both types were cycled at 2 mA cm^{-2} with a fixed capacity of 1mA h cm^{-2}. In **Figure 5**(d), the symmetrical battery with Ni_3S_2@Ni exhibits stable performance for nearly 900h without significant polarization. However, the symmetrical battery assembled with S-Ni 900 suffers from an overpotential increase

after 500 h. As shown in **Figure 5**(e), the overpotential of the S-Ni 900 collector electrode is up to 100 mV, much higher than the overpotential of the Ni_3S_2@Ni. The corresponding symmetrical batteries are further cycled for 40 h at current densities of 0.5, 1.0, 2.0 and 4.0 mA cm^{-2}, respectively, as shown in **Figure 5**(f). Clearly, the Ni_3S_2@Ni battery exhibits lower polarization values during the whole process. Even at 4.0 mA cm^{-2}, the voltage difference is approximately 50 mV, and the battery maintains normal operation at 0.5 mA cm^{-2}. In contrast, the polarization voltage of the S-Ni 900 battery increases rapidly, resulting in irreversible attenuation of the batteries. Severe lithium dendrites were generated on the surface of the electrode and pierced the separator at 4.0 mA cm^{-2}, suffering from short circuit of the battery. Hence, the Ni_3S_2@Ni current collector not only decrease the polarization of the battery, but also improves the battery cycling stability, which is much more promising than S-Ni 900 for Li metal battery operation.

3.4 Inhibition Mechanisms of Li Dendrite Growth During Cycling

Calculations of adsorption energy, based on density Functional Theory (DFT), are further performed to simulate the Li atoms absorption on the Ni backbone and Ni_3S_2 surfaces (**Figure 6**). As shown, the adsorption energy between the lithium atom and the Ni atom is -2.709 eV at the bottom of the Ni_3S_2 skeleton, -1.833 eV in the hollow position, and -3.009 eV on the top of the Ni_3S_2 skeleton. The adsorption energies of lithium atoms at the top, void and bottom positions of S-Ni-900 were -1.269 eV, -1.297 eV and -1.176 eV, respectively (Figure 6a-b), which were less than the adsorption energies of lithium at the corresponding positions of Ni_3S_2. This means that after surface modification, the Ni_3S_2@Ni current collector increased the adsorption tendency of lithium. Among these positions, lithium has a stronger adsorption preference in the top position on the Ni_3S_2 substrate. The strong adsorption between Ni_3S_2 and lithium promotes the preferential adsorption of lithium ions by the Ni_3S_2@Ni backbone. Benefiting from the Ni_3S_2@Ni lipophilicity, the lifespan and electrochemical performance in batteries can be impressive promoted [48].

Differences in morphology and composition will also affect the charge storage

performance, therefore, the differential charge density calculation and analysis method was adopted to obtain the basic information of the material in the bonding electron coupling process and the direction of bonding polarization [49-51]. As shown in Figure 6 (c-f), Ni_3S_2 is a hexagonal structure in which the S atom forms a slightly twisted body-centered cubic array, while the Ni atom occupies a twisted tetrahedral gap. The green, yellow, silver, red, and blue represents Li, S, Ni, accumulation of charge, and absence of charge, respectively. In the (110) crystal plane of Ni_3S_2, the density of electrons around Ni and S atoms is approximately spherical, and electrons accumulate between Ni and S along the bonding direction. Calculations show that the Li with the strongest adsorption energy in the two systems is 0.58 at the Ni (111) crystal plane, and the Bader charge value transferred at the Ni_3S_2 (110) crystal plane is 0.89. Apparently, compared with the S-Ni 900 skeleton collector, the 3D current collector material after *in-situ* growth of Ni_3S_2 has a higher Bader charge value, which is beneficial to the thin edge of the hexagonal nanosphere formed between the low coordination nickel atoms as the active site of ion adsorption. Furthermore, due to the increase in electron density, the vacancy adjustment may also lead to enhanced conductivity to reduce the charge-transfer resistance, thereby increasing its contact area with the electrolyte and improving lipophilicity.

3.5 Full Batteries Paired with $LiFePO_4$

To explore the practical feasibility of the Li/Ni_3S_2@Ni anode, full batteries were assembled and tested with a $LiFePO_4$ cathode. The full battery employed ether electrolyte and the voltage range is 2.4-4.2 V. As presented in Figure 7(a), under the current density of 1 C (1 C = 179 mA g^{-1}), the $LiFePO_4$|| Li@Ni_3S_2@Ni full cell displays a discharge capacity of 150.4 mAh g^{-1} in the first cycle. Furthermore, it has a remarkable capacity retention and unchanged voltage plateau in the following cycles. In Figure 7(b), the Li@bare Ni||LFP battery shows much faster capacity decay after 100 cycles. Figure 7(c) displays the cycling performance comparison of two full cells at a current density of 1C. As shown, the first discharge capacity of the $LiFePO_4$|| Li@Ni_3S_2@Ni is 151.89 mAh g^{-1}, while the $LiFePO_4$|| Li@ S-Ni 900 full battery is

143.16 mAh g^{-1}, respectively. After 500 cycles, $LiFePO_4$|| Li@1/24 Ni_3S_2@Ni full cell still maintains a specific capacity of 120 mAh g^{-1}, with an excellent capacity retention of 80.6%. In comparation, the specific capacity of the $LiFePO_4$|| Li@ S-Ni 900 full cell is only 105.95 mAh g^{-1}, and the capacity retention is only 74.1%. Figure 7(d) compares the rate performance of two batteries at 0.1 C, 0.5 C, 1.0 C, 2.0 C, and 5.0 C. At 0.1 C, the difference between two cells is subtle. However, as the discharge current increases, $LiFePO_4$||Li@1/24 Ni_3S_2@Ni full batteries exhibit much better electrochemical properties at 0.5 C, 1.0 C, 2.0 C, and 5.0 C. Thereby, these performances suggest that Ni_3S_2@Ni current collector realizes the lipophilic modification of the 3D nickel skeleton collector, reduces the nucleation overpotential, inhibits lithium dendrites, and enhances the cycle and rate efficiency of full cells.

4. Conclusion

In this work, we demonstrate a Ni_3S_2@Ni composite by a hydrothermal method to unlock the barrier of lithium metal batteries. The introduction of Ni_3S_2 improves the lipophilic properties of 3D porous nickel current collector, which facilitates the Li nucleation and plating process. Furthermore, the nano-porous structure with uniform composite collector is benefit to the migration and diffusion of Li^+, reduce the nucleation barrier, thereby prolonging the cycle life of batteries. On one hand, the symmetrical battery with Ni_3S_2@Ni exhibits stable performance for nearly 900h without significant polarization. On the other hand, the plating/stripping coulombic efficiency of the Ni_3S_2@Ni composite collector is as high as 98% at 2 mA cm^{-2} and at 1 mAh cm^{-2}, which exceeds the bare S-Ni 900 current collector. Moreover, the Ni_3S_2@Ni composite current collector results in promising performance in full cell systems. This Ni_3S_2@Ni composite current collector provides further insights to inhibit lithium dendrites and design long-life lithium metal batteries.

Acknowledgements

This work was supported by National Natural Science Foundation, China (Nos.

52071132, 52261135632 and U21A20284), Zhongyuan Thousand People Plan-The Zhongyuan Youth Talent Support Program (in Science and Technology), China (No. ZYQR201810139), Natural Science Foundation of Henan, China (Nos. 232300421080, 222300420138), Science and Technology Project of Henan Province, China (Nos. 232102241038, 232102241004), Key Scientific Research Programs in Universities of Henan Province， China－Special Projects for Basic Research (No. 23ZX008), Innovative Funds Plan of Henan University of Technology, China (No. 2020ZKCJ04). Dr. Xianyong Wu acknowledges the support from the NSF Center for the Advancement of Wearable Technologies (No.1849243).

References

1. X. Y. Li, C. J. Xue, Y. P. Liu, J. L. Zhao, J. W. Zhang, J. W. Zhang, *Electrochim. Acta*, 2023, **440**, 141697–141705.
2. L. M. Zhu, G. C. Ding, L. L. Xie, X. Y. Cao, J. P. Liu, X. F. Lei and J. X. Ma, *Chem. Mater.*, 2019, **31**, 8582−8612.
3. P. Qing, Z. B. Wu, A. B. Wang, S. Z. Huang, K. C. Long, T. Naren, D. P. Chen, P. He, H. F. Huang, Y. J. Chen, L. Mei and L. B. Chen, *Adv. Mater.*, 2023, **35**, 2211203.
4. J. Pang, M. J. Jia, Y. H. Zhang, J. H. Guo, Z. X. Shang, L. Tong, X. F. Gu, J. W. Zhang, *Ceram. Int.* 2023, **49**, 4531–4540.
5. C. J. Xue, Y. H. Zhang, Z. H. Nie, C. Q. Du, J. W. Zhang, J. W. Zhang, *Electrochim. Acta*, 2023, **444** 142021–142031.
6. A. Aribia, J. Sastre, X. Chen, M. H. Futscher, M. Rumpel, A. Priebe, M. Döbeli, N. Osenciat, A. N. Tiwari and Y. E. Romanyuk, *Adv. Energy Mater.*, 2022, **12,** 2201750.
7. H. Irfan and A. M. Shanmugharaj, *Appl. Surf. Sci.*, 2022, **586,**152806.
8. X. W. Shen, Y. T. Li, T. Qian, J. Liu, J. Q. Zhou, C. L. Yan and J. B. Goodenough, *Nat Commun*, 2019, **10**, 900.
9. J. Wang, H. Hu, S. Duan, Q. Xiao, J. Zhang, H. Liu, Q. Kang, L. Jia, J. Yang, W. Xu, H. Fei, S. Cheng, L. Li, M. Liu, H. Lin and Y. Zhang, *Adv. Funct. Mater.*, 2021, **32**, 2110468.
10. J. F. Ding, Y.T. Zhang, R. Xu, R. Zhang, Y. Xiao, S. Zhang, C. X. Bi, C. Tang, R. Xiang, H. S. Park, Q. Zhang and J.Q. Huang, *Green Energy & Environ.*, 2022, **8**, 2468-0257.

11. Y. Guo, S. Wu, Y.-B. He, F. Kang, L. Chen, H. Li and Q.H. Yang, *Science*, 2022, **2**, 138-163.
12. K.C. Pu, X. Zhang, X.L. Qu, J.J. Hu, H.W. Li, M.X. Gao, H.G. Pan and Y.F. Liu, *Rare Metals*, 2020, **39**, 616-635.
13. M. Gao, H. Li, L. Xu, Q. Xue, X. Wang, Y. Bai and C. Wu, *J. Energy Chem,* 2021, **59**, 666-687.
14. Y. Shi, B. Li, Y. Zhang, Y. Cui, Z. Cao, Z. Du, J. Gu, K. Shen and S. Yang, *Adv. Energy Mater.*, 2021, **11,** 2003663.
15. B. D. Adams, J. Zheng, X. Ren, W. Xu and J. G. Zhang, *Adv. Energy Mater.*, 2017, **8**,1702097.
16. J. Xiao, Q. Y. Li, Y. J. Bi, M. Cai, B. Dunn, T. Glossmann, J. Liu, T. Osaka, R. Sugiura and B. B. Wu, *Nat. Energy.*, 2020, **5**, 561−568.
17. Y. Niu, L. L. Xie, T. Zhou, J. Xu, Y. C. Ding, Q, Han, X. J. Qiu, Y. M. Xiao, Y. X. Miao, L. M. Zhu and X. Y. Cao, *ACS App. Nano Mater.*, 2022, **6**, 622−632.
18. L. M. Zhu, G. C. Ding, Q. Han, Y. X. Miao, X. Lin, X. L. Yang, L. Chen, G. K. Wang, L. L. Xie and X. Y. Cao, *Rare Metals.*, 2021, **41**, 425−437.
19. J. L. Fu, X. Ji, J. Chen, L. Chen, X. L. Fan, D. B. Mu and C. S. Wang, *Angew. Chem. Int. Edit.*, 2020, **59**, 22194−22201.
20. N. Piao, X. Ji, H. Xu, X. L. Fan, L. Chen, S. F. Liu, M. N. Garage, S. C. Greenbaum, L. Wang, C. S. Wang and X. M. He, *Adv. Energy Mater.*, 2020, **10**, 1903568.
21. Q. K. Zhang, X. Q. Zhang, H. Yuan and J. Q. Huang, *Small Sci.*, 2021, **1**, 2170025.
22. H. Zheng, H. F. Xiang, F. Y. Jiang, Y. C. Liu, Y. Sun, X. Liang, Y. Z. Fang and Y. Yu, *Adv. Energy Mater.*, 2020, **10**, 2001440.
23. J. Q. Dai, C. P. Yang, C. W. Wang, G. Pastel and L. B. Hu, *Adv. Mater.*, 2018, **30**, 1802068.
24. Q. Ma, X. X. Zeng, J. P. Yue, Y. X. Yin, T. T. Zuo, J. Y. Liang, Q. Deng, X. W. Wu and Y. G. Guo, *Adv. Energy Mater.*, 2019, **9**, 1803854.
25. B. Zhao, W. C. Ma, B. B. Li, X. T. Hu, S. Y. Lu, X. Y. Liu, Y. Jiang and J. J. Zhang, *Nano Energy.*, 2022, **91**, 106643.
26. Y. Liu, Y. P. Zhai, Y. Y. Xia, W. Li and D. Y. Zhao, *Small Struct.*, 2021, **2**, 2000118.
27. F. Pei, A. Fu, W. Ye, J. Peng, X. Fang, M. S. Wang and N. Zheng, *ACS Nano*, 2019, **13**, 8337-8346.
28. D. Zhang, A. Dai, M. Wu, K. Shen, T. Xiao, G. Y. Hou, J. Lu and Y. P. Tang, *ACS Energy Lett.*, 2019, **5**, 180−186.

29. K. Q. Qin, K. Holguin, M. Mohammadiroudbari, J. H. Huang, E. Y. S. Kim, R. Hall and C. Luo, *Adv. Funct. Mater.*, 2021, **31**, 2009694.

30. J. M. Wang, B. C. Ge, H. Li, M. Yang, J. Wang, D. Liu, C. Fernandez, X. B. Chen and Q. M. Peng, *Chem. Eng. J.*, 2021, **420**, 129739.

31. Y. J. Fang, S. L. Zhang, Z. P.W u, D. Y. Luan, *Sci. Adv.* , 2021, **7,** 3626.

32. G. X. Lu, J. W. Nai, D. Y. Luan, X. Y. Tao, *Sci. Adv.* , 2023, **9**, 1550.

33. Y. J. Liu, X. Y. Tao, Y. Wang, C. Jiang, C.Ma, G. X. Lu, X. W. Lou, *Science*, 2022, **375**, 739–745.

34. R. Zhang, S. W. Wen, N. Wang, K. Q. Qin, E. Z. Liu, C. S. Shi and N. Q. Zhao, *Adv. Energy Mater.*, 2018, **8,** 1800914.

35. Z. L. Hu, Z. Z. Li, Z. Xia, T. Jiang, G. L. Wang, J. Y. Sun, P. F. Sun, C. L. Yan and L. Zhang, *Energy Storage Mater.*, 2019, **22**, 29−39.

36. R. Li, J. X. Wang, L. D. Lin, H. Wang, C. M. Wang, C. H. Zhang, C. H. Song, F. Tian, J. Yang and Y. T. Qian, *Mater. Today Energy.*, 2020, **15,** 100367.

37. N. Li, K. Zhang, K. Y. Xie, W. F. Wei, Y. Gao, M. H. Bai, Y. L. Gao, Q. Hou, C. Shen, Z. H. Xia and B. Q. Wei, *Adv. Mater.*, 2020, **32**, 1907079.

38. P. Shi, T. Li, R. Zhang, X. Shen, X. B. Cheng, R. Xu, J. Q. Huang, X. R. Chen, H. Liu and Q. Zhang, *Adv. Mater.*, 2019, **31**, 1807131.

39. R. Jiang, Y. D. Song and P. A. Reed, *Int. J. Fatigue.*, 2020, **141**, 105887.

40. N. Wang, G. Y. Han, Y. Z. Chang, W. J. Hou, Y. M. Xiao and H. G. Li, *Electrochem. Acta.*, 2019, **317,** 322−332.

41. X. L. Yin, S. R. Yu, Y. Zhao, E. Y. Liu and K. Wang, *J. Taiwan Inst. Chem. E.*, 2019, **99,** 268−275.

42. S. Wang, J. G. Tu, J. S. Xiao, J. Zhu and S. Q. Jiao, *J. Energy Chem.*, 2019, **28**, 144−150.

43. J. Chen, Q. Li, T. P. Pollard, X. L. Fan, O. Borodin and C. S. Wang, *Mater. Today.*, 2020, **39,** 118−126.

44. K. H. Chen, K. N. Wood, E. Kazyak, W. S. LePage, A. L. Davis, A. J. Sanchez and N. P. Dasgupta, *J. Mater. Chem. A*, 2017, **5,** 11671−11681.

45. R. J. Zhu, H. J. Yang, L. Fadillah, Z. T. Xiong, D. Kowalski, C. Y. Zhu, S. Kitano, Y. Aoki and H. Habazaki, *J. Mater. Chem. A*, 2021, **9**, 13332−13343.

46. C. Chen, J. Guan, N. W. Li, Y. Lu, D. Y. Luan, C. H. Zhang, G. Cheng, L. Yu and X. W. Lou, *Adv.*

Mater.,2021, **33,** 2100608.

47. S. Zhang, W. Deng, X. Zhou, B. He, J. Liang, F. Zhao, Q. Guo and Z. Liu, *Mater. Today Energy.*, 2021, **21**, 100770.
48. D. J. Zhu, S. F. Li, J. T. Huang, Z. Chen, Z. H. Hu, J. Li, X. B. Li, H. Y. Yang and Z. J. Feng, *J. Alloy. Compd.*, 2021, **859,** 158246.
49. R. Lu, B. Zhang, Y. Cheng, K. Amin, C. Yang, Q. Zhou, L. Mao and Z. Wei, *J. Mater. Chem. A*, 2021, **9**, 10393-10403.
50. B. Sun, Q. Zhang, W. Xu, R. Zhao, H. Zhu, W. Lv, X. Li and N. Yang, *Nano Energy*, 2022, **94,** 2211-2855.
51. N. Zheng, C. Liang, C. Wu, X. Zhang, W. Zhai, M. Liu, H. Wei, C. Zhang, L. Dong, Y. Yu, W. Liu and L. Yao, *J. Mater. Chem. A*, 2022, **10**, 5391-5401.

Figure captions

Figure 1. (a) The scheme of the fabrication and the Li plating/stripping process on the Ni_3S_2@Ni composite current collector. (b) The Li plating/stripping process on the S-Ni 900 current collector.

Figure 2. (a)XRD results of the obtained the S-Ni 900 current collector and Ni_3S_2@Ni composite current collector. (b) XPS energy spectra for S-Ni 900 and 1/24 Ni_3S_2@Ni composite collectors, (c) Ni energy spectra for S-Ni 900, (d) S elemental spectra for 1/24 Ni_3S_2@Ni composite fluid collectors, and (e) Ni element energies for 1/24 Ni_3S_2@Ni composite collectors.

Figure 3. Structural characterization of the S-Ni 900 current collector and Ni_3S_2@Ni composite current collector: SEM images at different magnifications for the S-Ni 900 current collector and Ni_3S_2@Ni composite current collector.

Figure 4. SEM images of the morphologies of two current collectors in symmetrical cells after different cycles. (a) SEM of 1/24 Ni_3S_2@Ni composite current collector in a symmetrical battery after different cycles. (b) SEM of Ni current collector in a symmetrical battery after different cycles. (c) The cross-sectional SEM images of the S-Ni 900 current collector (A-C) and Ni_3S_2@Ni composite current collector (D-F) after different cycles: A and D SEM of initially deposited lithium, B and E SEM after 1 cycle, C and F SEM after 45 cycles.

Figure 5. (a) S-Ni 900 and 1/24 Ni_3S_2@Ni composite current collector lithium deposition capacity-voltage curve. Voltage profiles of Li plating/stripping at 1 mA cm^{-2}, at 1 mA h cm^{-2} on (b) S-Ni 900 substrate and (c) the 1/24 Ni_3S_2@Ni substrate. (d) Symmetrical cells performance of S-Ni 900 substrate and 1/24 Ni_3S_2@Ni composite current collector. (e) Partial enlargement of curve (f) Rate performance of symmetrical cells assembled with 1/24 Ni_3S_2@Ni composite collector and S-Ni 900 current collector.

Figure 6. (a) Calculations of adsorption energies of a Li atom on the surface of Ni (b) and Ni_3S_2 (c-d) Ni and (e-f) Ni_3S_2 charge differential density plot.

Figure 7. Electrochemical performance comparison of the Li/ 1/24 Ni_3S_2@Ni |LFP and Li/S-Ni-900|LFP batteries. (a and b) Voltage profiles of the Li/ 1/24 Ni_3S_2@Ni |LFP and Li/ S-Ni-900|LFP. (c) Cycling performance of the full cells at the rate of 1 C. (d) Different rates of the full cells from 0.1 to 5 C.

Figure 1.

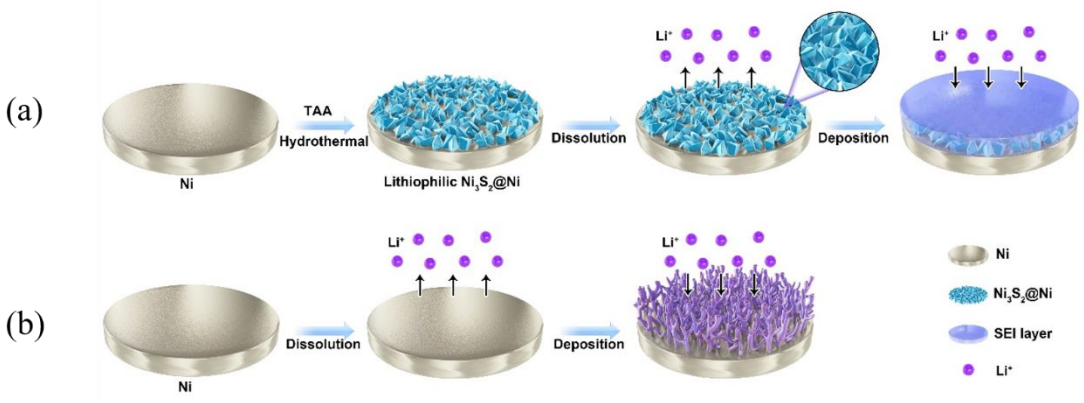
(a)
Ni
TAA
Hydrothermal
Lithiophilic Ni3S2@Ni
Dissolution
Li+
Deposition
Li+
(b)
Ni
Dissolution
Li+
Deposition
Li+
Ni
Ni3S2@Ni
SEI layer
Li+

Figure 2.

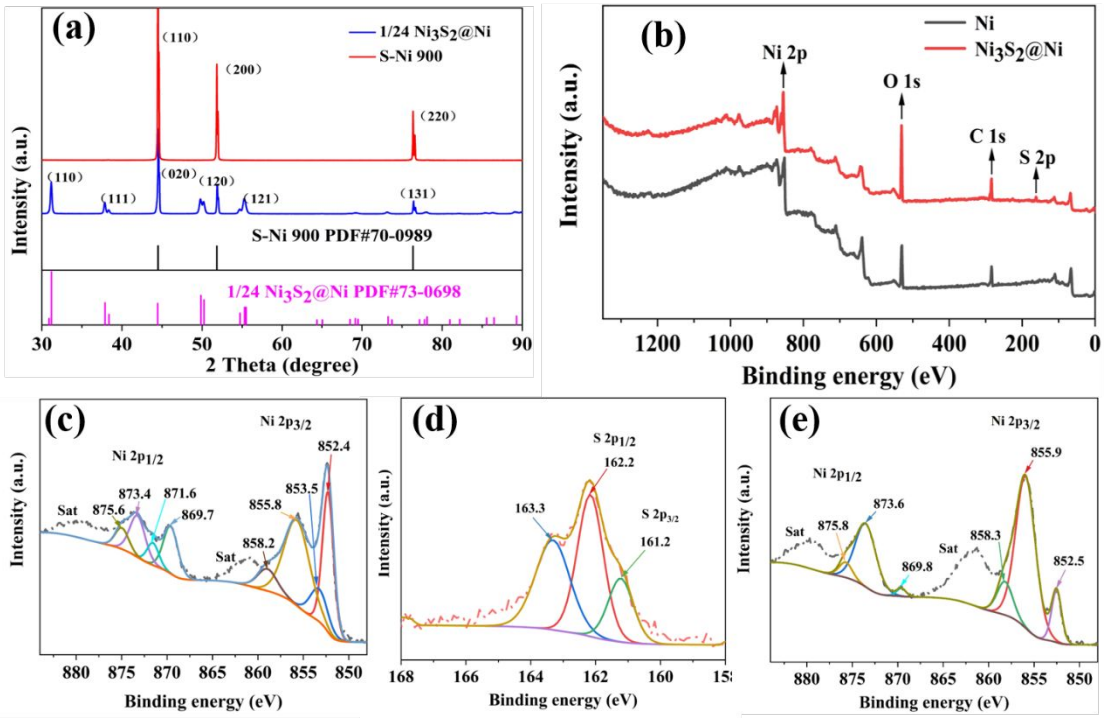
(a)
1/24 Ni3S2@Ni
S-Ni 900
(110)
(200)
(220)
(110)
(111)
(020)
(120)
(121)
(131)
S-Ni 900 PDF#70-0989
1/24 Ni3S2@Ni PDF#73-0698
Intensity (a.u.)
2 Theta (degree)
(b)
Ni
Ni3S2@Ni
Ni 2p
O 1s
C 1s
S 2p
Intensity (a.u.)
Binding energy (eV)
(c)
Ni 2p3/2
Ni 2p1/2
852.4
873.4
871.6
853.5
Sat
875.6
869.7
855.8
858.2
Sat
Intensity (a.u.)
Binding energy (eV)
(d)
S 2p1/2
162.2
163.3
S 2p3/2
161.2
Intensity (a.u.)
Binding energy (eV)
(e)
Ni 2p3/2
855.9
Ni 2p1/2
873.6
Sat
875.8
858.3
Sat
869.8
852.5
Intensity (a.u.)
Binding energy (eV)

Figure 3.

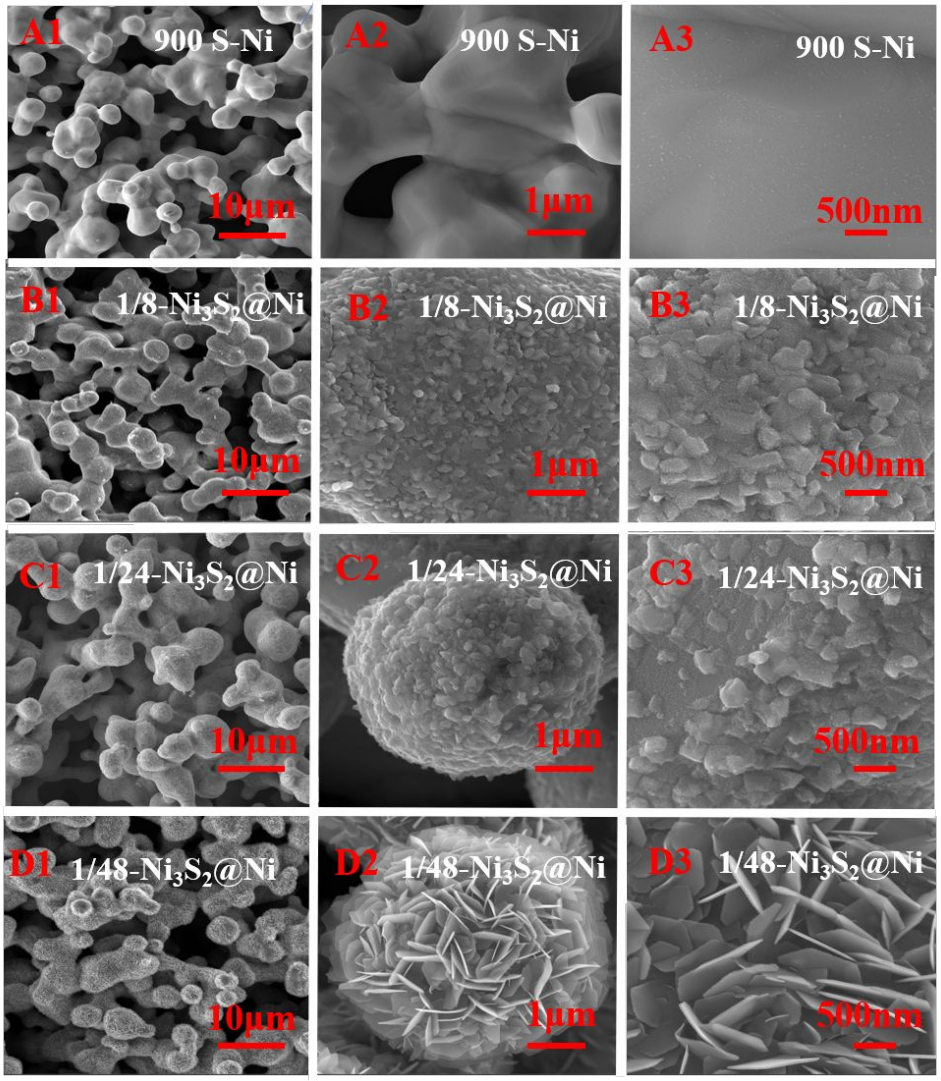
A1
900 S-Ni
10μm
A2
900 S-Ni
1μm
A3
900 S-Ni
500nm
B1
1/8-Ni3S2@Ni
10μm
B2
1/8-Ni3S2@Ni
1μm
B3
1/8-Ni3S2@Ni
500nm
C1
1/24-Ni3S2@Ni
10μm
C2
1/24-Ni3S2@Ni
1μm
C3
1/24-Ni3S2@Ni
500nm
D1
1/48-Ni3S2@Ni
10μm
D2
1/48-Ni3S2@Ni
1μm
D3
1/48-Ni3S2@Ni
500nm

Figure 4.

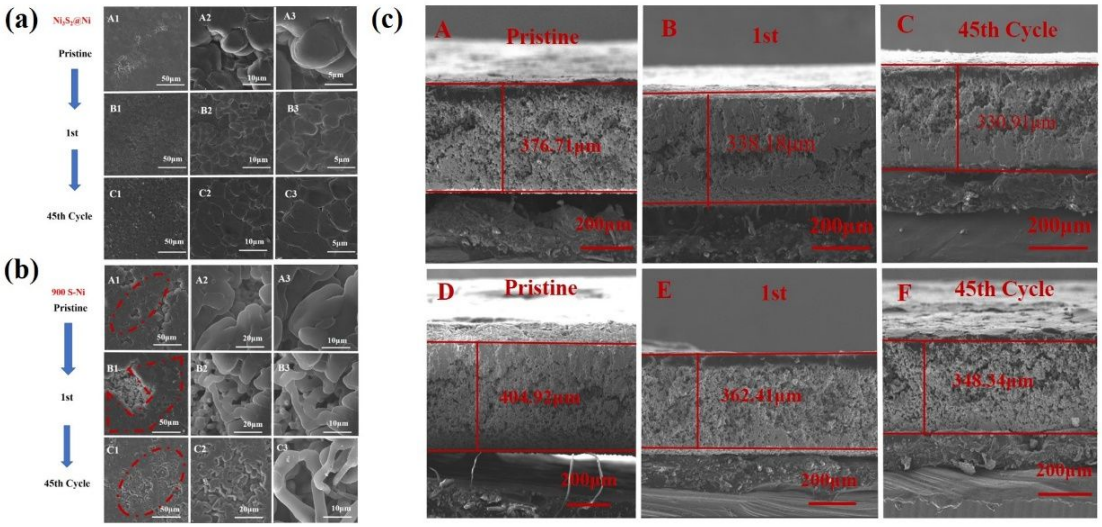
(a)
Ni3S2@Ni
Pristine
1st
45th Cycle
A1
A2
A3
B1
B2
B3
C1
C2
C3
(b)
900 S-Ni
Pristine
1st
45th Cycle
(c)
A Pristine
376.71μm
B 1st
338.18μm
C 45th Cycle
330.91μm
D Pristine
404.92μm
E 1st
362.41μm
F 45th Cycle
348.54μm
200μm

Figure 5.

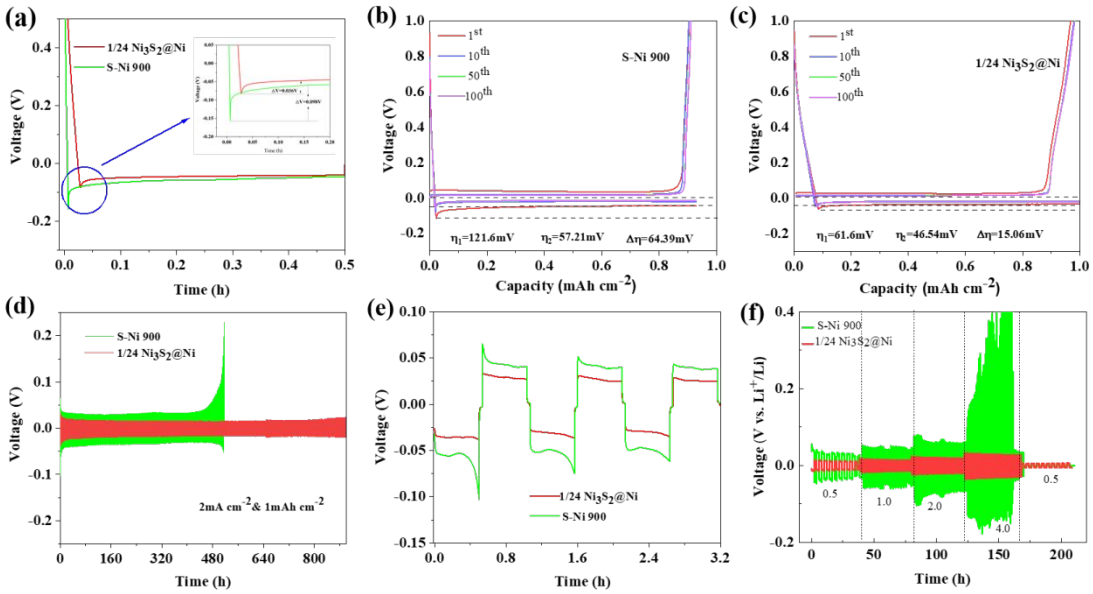
(a)
1/24 Ni3S2@Ni
S-Ni 900
Voltage (V)
Time (h)
(b)
1st
10th
50th
100th
S-Ni 900
η1=121.6mV
η2=57.21mV
Δη=64.39mV
Voltage (V)
Capacity (mAh cm-2)
(c)
1st
10th
50th
100th
1/24 Ni3S2@Ni
η1=61.6mV
η2=46.54mV
Δη=15.06mV
Voltage (V)
Capacity (mAh cm-2)
(d)
S-Ni 900
1/24 Ni3S2@Ni
2mA cm-2& 1mAh cm-2
Voltage (V)
Time (h)
(e)
1/24 Ni3S2@Ni
S-Ni 900
Voltage (V)
Time (h)
(f)
S-Ni 900
1/24 Ni3S2@Ni
0.5
1.0
2.0
4.0
0.5
Voltage (V vs. Li+/Li)
Time (h)

Figure 6.

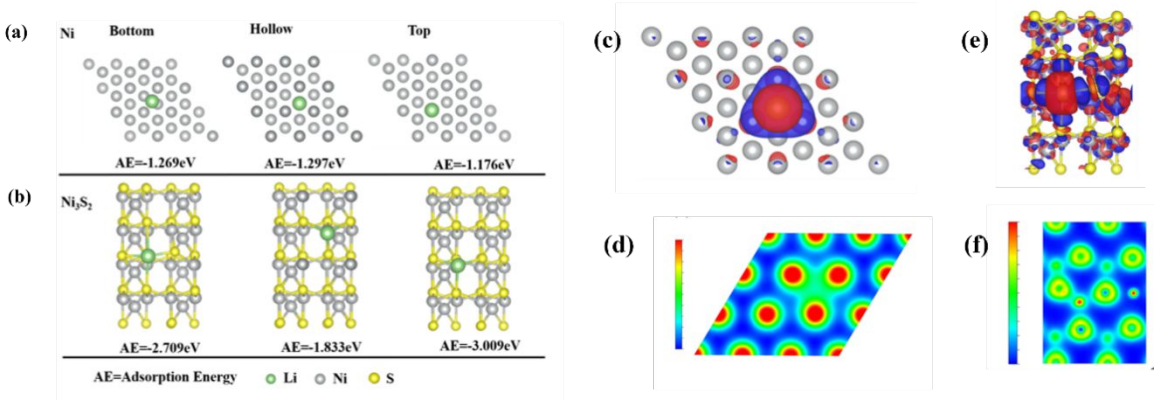
(a)
Ni
Bottom
Hollow
Top
AE=-1.269eV
AE=-1.297eV
AE=-1.176eV
(b)
Ni_3S_2
AE=-2.709eV
AE=-1.833eV
AE=-3.009eV
AE=Adsorption Energy
Li
Ni
S
(c)
(d)
(e)
(f)

Figure 7.

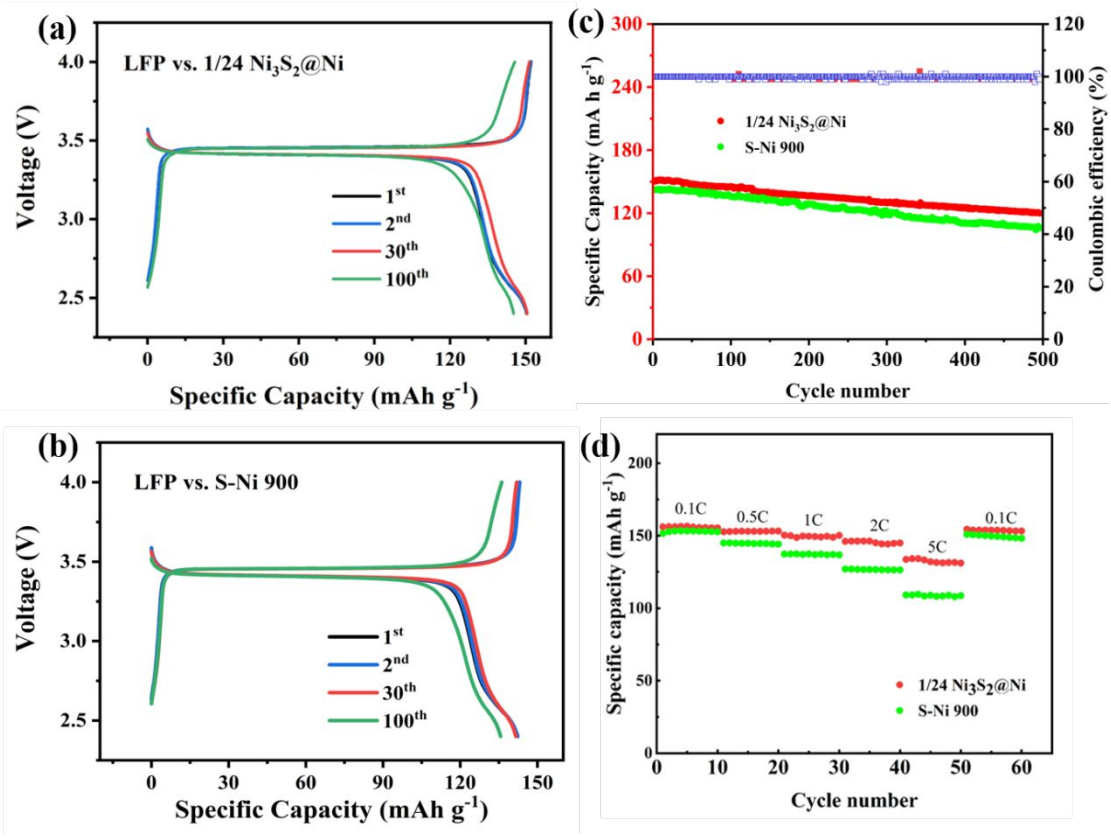
(a)
LFP vs. 1/24 Ni3S2@Ni
Voltage (V)
Specific Capacity (mAh g-1)
1st
2nd
30th
100th
(b)
LFP vs. S-Ni 900
Voltage (V)
Specific Capacity (mAh g-1)
1st
2nd
30th
100th
(c)
Specific Capacity (mA h g-1)
Coulombic efficiency (%)
Cycle number
1/24 Ni3S2@Ni
S-Ni 900
(d)
Specific capacity (mAh g-1)
Cycle number
0.1C
0.5C
1C
2C
5C
0.1C
1/24 Ni3S2@Ni
S-Ni 900